

Something something something physics

Steven Green
of Emmanuel College

A dissertation submitted to the University of Cambridge
for the degree of Doctor of Philosophy

Abstract

This thesis describes the optimisation of the calorimeter design for collider experiments at the future Compact Linear Collider (CLIC) and the International Linear Collider (ILC). The detector design of these experiments is built around high-granularity Particle Flow Calorimetry that, in contrast to traditional calorimetry, uses the energy measurements for charged particles from the tracking detectors. This can only be realised if calorimetric energy deposits from charged particles can be separated from those of neutral particles. This is made possible with fine granularity calorimeters and sophisticated pattern recognition software, which is provided by the PandoraPFA algorithm. This thesis presents results on Particle Flow calorimetry performance for a number of detector configurations. To obtain these results a new calibration procedure was developed and applied to the detector simulation and reconstruction to ensure optimal performance was achieved for each detector configuration considered.

This thesis also describes the development of a software compensation technique that vastly improves the intrinsic energy resolution of a Particle Flow Calorimetry detector. This technique is implemented within the PandoraPFA framework and demonstrates the gains that can be made by fully exploiting the information provided by the fine granularity calorimeters envisaged at a future linear collider.

A study of the sensitivity of the CLIC experiment to anomalous gauge couplings that effect vector boson scattering processes is presented. These anomalous couplings provide insight into possible beyond standard model physics. This study, which utilises the excellent jet energy resolution from Particle Flow Calorimetry, was performed at centre-of-mass energies of 1.4 TeV and 3 TeV with integrated lumi-

nosities of 1.5ab^{-1} and 2ab^{-1} respectively. The precision achievable at CLIC is shown to be approximately one to two orders of magnitude better than that currently offered by the LHC.

Finally, a study into various technology options for the CLIC vertex detector is described.

Declaration

This dissertation is the result of my own work, except where explicit reference is made to the work of others, and has not been submitted for another qualification to this or any other university. This dissertation does not exceed the word limit for the respective Degree Committee.

Andy Buckley

Acknowledgements

Of the many people who deserve thanks, some are particularly prominent, such as my supervisor...

Preface

This thesis describes my research on various aspects of the LHCb particle physics program, centred around the LHCb detector and LHC accelerator at CERN in Geneva.

For this example, I'll just mention Chapter ?? and Chapter ??.

Contents

1	Reconstruction Chain	1
1.1	Reconstruction Chain	1
1.2	Event Generation, Simulation and Reconstruction	1
2	Calorimeter Optimisation Studies	3
2.1	Calorimeter Optimisation Studies	3
2.2	Jet Energy Resolution	4
2.2.1	Jet Energy Resolution Metrics	5
2.2.2	Jet Energy Resolution Decompositions	6
2.2.3	Single Particle Energy Resolution	7
2.3	Nominal Detector Performance	8
2.4	Electromagnetic Calorimeter Optimisation	13
2.4.1	ECal Transverse Segmentation	14
2.4.2	ECal Number of Layers	16
2.4.3	ECal Active Material	19
2.5	Hadronic Calorimeter Optimisation	20
2.5.1	HCal Absorber Material	21
2.5.2	HCal Transverse Segmentation	23
2.5.3	HCal Number of Layers	25
2.5.4	HCal Sampling Fraction	27
2.5.5	HCal Sampling Frequency	27
2.6	Global Detector Parameters	30
2.6.1	The Magnetic Field Strength	31
2.6.2	Inner ECal Radius	33
2.7	Conclusions	34
	Bibliography	37
	List of figures	39

List of tables

43

*“Writing in English is the most ingenious torture
ever devised for sins committed in previous lives.”*

— James Joyce

Chapter 1

Reconstruction Chain

“There, sir! that is the perfection of vessels!”

— Jules Verne, 1828–1905

1.1 Reconstruction Chain

1.2 Event Generation, Simulation and Reconstruction

The jet fragmentation and hadronisation for the $Z \rightarrow uds$ events used for determining the metric for detector performance was controlled using PYTHIA [11] that had been tuned using data from LEP [4]. Single particle spatially isotropic samples of K_L^0 , γ and μ^- were produced for the calibration of each detector model. A simple c++ script was written to generate the relevant HEPEvt common blocks for these samples.

Detector model simulation was performed using MOKKA [9], a GEANT4 [3] wrapper providing detailed geometric descriptions of detector concepts for the linear collider. Event reconstruction was performed using MARLIN [6], a c++ framework designed for reconstruction at the linear collider. PandoraPFA [8,12] was used to apply Particle Flow Calorimetry in the reconstruction, the full details of which can be found in chapter PANDORA CHAPTER.

Chapter 2

Calorimeter Optimisation Studies

“The simple believes everything, but the prudent gives thought to his steps.”

— Proverbs 14:15

2.1 Calorimeter Optimisation Studies

The fundamental principle of particle flow calorimetry is to measure the energy of a particle passing through a detector in whichever sub-detector offers the best energy resolution. For particle colliders experiments, this involves measuring the momenta of charged particles using the curvature of the track they create in the detector. This offers extremely good energy resolution in comparison to calorimetric energy measurements and is the source of the excellent energy resolution particle flow calorimetry can produce. As neutral particles produce no tracks, their energies must be measured using calorimetric energy deposits.

The application of particle flow calorimetry is extremely challenging as it is possible, by using incorrect associations of charged particle tracks to calorimetric energy deposits, to both double count and omit energy measurements. For example, if a charged particle calorimetric energy deposit is not associated to a track that energy deposit will be double counted, while if a neutral particle calorimetric energy deposit is associated to a track that energy deposit will be neglected. Therefore, making the correct associations between charged particle tracks and calorimetric energy deposits is essential.

These associations can only be successfully made if the calorimeters in use have fine segmentation, such as those found at the linear collider experiment, so that it becomes possible to separate the energy deposits from nearby showering particles. Even with this segmentation making the association of charged particle tracks to the calorimetric energy deposits is highly non-trivial. At the linear collider experiment, these associations are made using sophisticated pattern recognition algorithms, provided by PandoraPFA. The fine segmentation of the calorimeters allows PandoraPFA to reconstruct the four-momenta of all particles passing through the detector and to use the energy measurement from the optimal sub-detector in each case.

In this chapter optimisation of the calorimeters used at the linear collider, with focus placed on obtaining the best energy resolution for jets, is considered. Parameters such as the number of layers, transverse segmentation and material choices for the calorimeters are considered.

This chapter concludes with an optimisation of several global parameters for the detector such as the magnetic field strength used for the detector and the inner radius of the ECal. These parameters are not calorimeter specific, but affect the jet energy resolution obtained from particle flow.

2.2 Jet Energy Resolution

As many physics processes of interest at the linear collider involve multi-jet final states, good jet energy resolution is a crucial aspect of detector performance. As shown in chapter PHYSICS ANALYSIS, parameters derived from the energy measurements of jets, such as invariant mass, are extremely useful for identification of physics channels of interest as well as determining the sensitivity of the linear collider experiments to areas of new physics. Therefore, the primary metric used in this study is the jet energy resolution.

Jet energy resolution in particular can benefit from the application of particle flow calorimetry as $\approx 70\%$ of the energy of jets are carried in the form of charged particles. As particle flow aims to measure the energy of charged particles using the tracker, it has the potential to offer extremely large benefits when measuring jet energies in comparison to the traditional calorimetric approach.

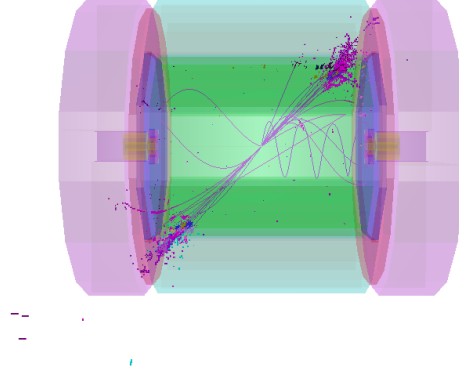


Figure 2.1: 500 GeV di-jet $Z \rightarrow uds$ event display for nominal ILD detector.

2.2.1 Jet Energy Resolution Metrics

The primary metric used to optimise detector performance is the jet energy resolution. This was found through the simulation of off-shell mass Z boson events decaying to light quarks (u, d, s). In these events the Z boson is produced at rest, which means the typical decays form two mono-energetic jets that are produced back to back as shown in figure 2.1. Only events where $|\cos(\theta)| < 0.7$, where θ is the polar angle of the quarks from the Z decay, are used in the metric calculation to ensure little energy is lost down the beam axis. Using these events the jet energy resolution is calculated as follows:

$$\frac{\text{RMS}_{90}(E_i)}{\text{Mean}_{90}(E_i)} = \frac{\text{RMS}_{90}(E_{jj})}{\text{Mean}_{90}(E_{jj})} \times \sqrt{2}, \quad (2.1)$$

where $\text{RMS}_{90}(E_{jj})$ and $\text{Mean}_{90}(E_{jj})$ are the root mean squared (RMS) and the mean of the reconstructed energy distribution calculated within the range of with the smallest RMS containing at least 90% of the data. respectively.

This definition is used to remove the effect of outliers in the distribution [12]. Although the correct combination of charged particle tracks and calorimetric energy measurements would give a Gaussian reconstructed jet energy distribution, the effect of confusion on certain events will distort this distribution and broaden the tails significantly. If the full range were to be used in the jet energy resolution calculation, the effect of these tails is overinflated. If the distribution of reconstructed jet energies

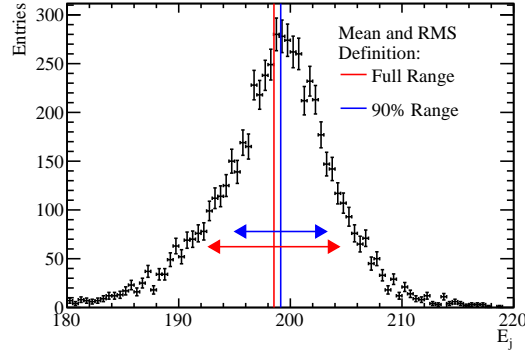


Figure 2.2: Definition of jet energy resolution. Reconstructed jet energy for 200 GeV di-jet $Z \rightarrow uds$ events for nominal ILD detector.

is truncated to the narrowest range of the data containing at least 90% of the data, the effect of these tails can be negated. This removes events where confusion is dominant, which makes the jet energy resolution metric far more robust and representative of the bulk of the data.

An example of the application of this metric can be found in figure 2.2. The RMS calculated using the full range 5.8 GeV, while the RMS using the reduced range is 4.1 GeV. This corresponds to a reduction in the jet energy resolution from 4.1% to 2.9%, which clearly shows an overemphasis of the tails of the distribution if the full range is used in the calculation.

In the subsequent analysis a range of di-jet energies were considered ranging from the Z mass, 91 GeV, to the nominal running energy of the ILC, 500 GeV. Each event sample contained 10,000 events generated spatially isotropically so that, given the polar angle cut, approximately 7,000 events contribute to the jet energy resolution metric.

2.2.2 Jet Energy Resolution Decompositions

The pattern recognition performed for the linear collider experiments is full described in section PANDORA SECTION, however, it is possible to gain further insight into the detector performance by cheating various parts of the pattern recognition using the MC information. Pattern recognition confusion manifests itself on energy measurements in two ways:

- If part of the calorimetric energy deposit from a charged particle is not associated to the track that energy deposit is double counted.
- If part of the calorimetric energy deposit from a neutral particle is incorrectly associated to a track, the energy deposit is not accounted for.

Both of these sources of confusion lead to inaccurate measurements of the jet energy and thus degrade the resolution. Cheating the pattern recognition, therefore, removes the effects of confusion and improves the detector performance.

The intrinsic energy resolution contribution to the jet energy resolution was determined by fully cheating the pattern recognition; in this case all confusion is negated. The total confusion is defined as the quadrature difference between the jet energy resolution using the standard reconstruction and this fully cheated reconstruction. Furthermore, it is possible to cheat the pattern recognition associated with individual types of particles. This is particularly useful for studies related to the ECal as, by cheating the photon pattern recognition, it is possible to isolate the confusion associated with photons. The photon confusion is defined as the quadrature difference between the jet energy resolution using the standard reconstruction and the reconstruction where photons pattern recognition is cheated.

2.2.3 Single Particle Energy Resolution

Several physics studies rely on the identification of single particles, such as γ in anomalous triple gauge coupling studies CITE, and as such the energy resolution of individual particles is presented alongside the jet energy resolution metric. As only uncharged particle energies are measured in the calorimeters in the particle flow paradigm, the single particle energy resolution is shown using γ s and for K_L^0 s. γ s are particularly relevant for several physics studies and, as they are largely contained within the ECal, they provide insight into detector changes related purely to the ECal. This makes γ s a natural choice of particle to consider for this study. K_L^0 s were used as, analogously to γ s and the ECal, their energies are primarily measured using the HCal. Although in general neutral hadron energy resolutions are less crucial to physics studies, the energy resolution is still a crucial contribution to the jet energy resolution, which should not be overlooked. For these single particle samples the energy resolution is defined using a Gaussian fit to the reconstructed energy distributions. The fit was applied to the narrowest region of the reconstructed

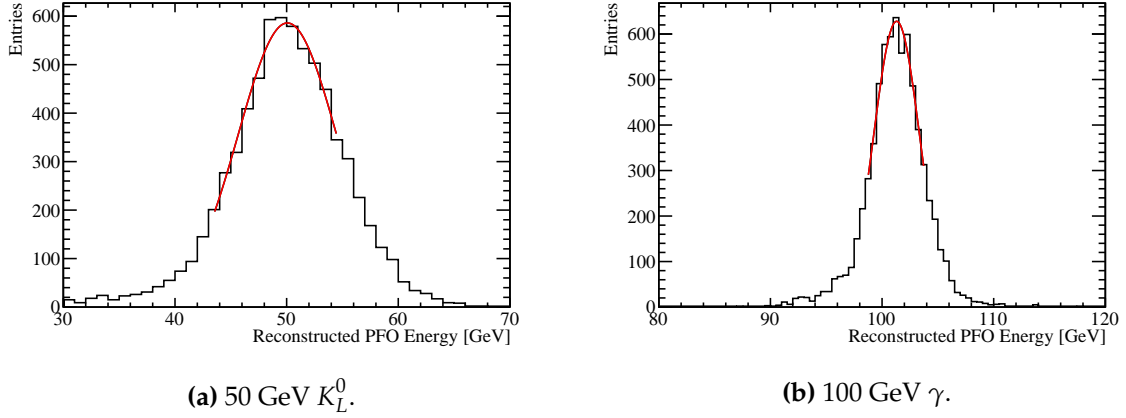


Figure 2.3: The reconstructed energy distribution for (a) 50 GeV K_L^0 and (b) 100 GeV γ events. The red line shows a Gaussian fit used to parameterise the detector performance. The fit was applied to the truncated range of the reconstructed PFO energy distribution containing at least 75% of the data with the narrowest RMS. The nominal ILD model was used in this simulation.

PFO energy distribution that contained at least 75% of the data. This increases the likelihood that the fit converges and ensures a better parameterisation of the bulk of the data set. The resolution is defined as the standard deviation divided by the mean of that reconstructed Gaussian. A total of 10,000 events are used to calculate the energy resolution at each fixed energy point. A cut of $|\cos(\theta)| < 0.7$ is applied to ensure events avoid the Barrel/EndCap overlap region. Examples of the single particle energy distributions for 100 GeV γ s and 50 GeV K_L^0 s alongside the Gaussian fit used to determine their energy resolution are shown in figure 2.3. The errors quoted on single particle energy resolutions are determined by propagating the errors reported from the Gaussian fit into the resolution calculation.

2.3 Nominal Detector Performance

Before addressing the optimisation of the detectors for use at a future linear collider is it necessary to properly quantify the behaviour of the nominal detector model that is used in the simulations. For these studies the nominal ILD model is used.

The calorimeters at a linear collider are sampling calorimeters, therefore, the reconstructed energy distributions for neutral particles whose energies are measured in the calorimeters will be Gaussian. This is expected due as the active material for

each calorimeter cell essentially counts the number of charged particle tracks passing through it, or possible the number of photons for scintillator options. The working hypothesis for estimating the energy deposited in a sampling calorimeter is that the energy of a showering particle is proportional to the number of charged particle tracks, or photons for scintillator detector options, it produces. Having counted the number of tracks in the active region of the calorimeter cell it is possible to estimate the energy deposited in the whole calorimeter cell in the digitisation process, further details on this can be found in chapter CALIBRATION CHAPTER. Finally, the energy of the entire particle shower is estimated by grouping the calorimeter cells and summing their energy. Each calorimeter cell energy is an independently random measurements and, by the central limit theorem CITE, the sum of a large number of independently random measurements has a Gaussian distribution. It follows that the variance of the shower energy distribution is given by the sum of the variances for each of the calorimeter cell energy distributions.

As each calorimeter hit involves counting a number of objects, charged particle tracks or photons, the statistics governing the distribution of the individual cell energies are Poisson statistics. For a given particle shower, if the mean of a cell energy is given by $\lambda = N$ where N is the mean number of objects that are expected, the standard deviation of that distribution is $\sigma = \sqrt{\lambda} = \sqrt{N}$ and the energy resolution $\frac{\sigma}{\lambda} = \frac{1}{\sqrt{N}}$. As the total shower energy, E_{Reco} , is proportional to N_{Reco} , the total number of tracks recorded in the calorimeter, the energy resolution for an ideal calorimeter is proportional to $\frac{1}{\sqrt{N_{Reco}}} = \frac{1}{\sqrt{E_{Reco}}}$. This gives the form of the energy resolution as a function of energy for an ideal calorimeter as $\frac{\sigma_{Reco}}{E_{Reco}} = \frac{a}{\sqrt{E_{Reco}}}$. In reality, it is typical to express the energy resolution of a calorimeter in the following form

$$\frac{\sigma_{Reco}}{E_{Reco}} = \frac{a}{\sqrt{E_{Reco}}} \oplus b \oplus \frac{c}{E_{Reco}}, \quad (2.2)$$

where the b term is a constant term that accounts for a variety of effects such as CHECK and the c term accounts for electrical noise.

Prototypes of the various ILD calorimeter options have been constructed and validated using test beam. The energy resolution measured using the test beam was parameterised as $\frac{16.6}{\sqrt{E_{Reco}}} \oplus 1.1\%$ for the silicon ECal and $\frac{12.9}{\sqrt{E_{Reco}}} \oplus 1.2\%$ for the scintillator ECal [1]. The electrical noise was deemed sufficiently small that the c term in

the parameterisation could be neglected in both cases. These results were determined using an e^- test beam with energies ranging up to ≈ 40 GeV. This parameterisation is compared to the results found using the full ILD detector simulation in figures 2.4a and 2.4b for the silicon and scintillator ECal options respectively. The parameterisation of the energy resolution for the silicon ECal option is almost identical to the energy resolution results when using the full ILD simulation. However, for the scintillator ECal option the parameterisation is significantly better than that observed in the full simulation. This difference is most likely due to an imperfect implementation of the scintillator ECal within the full detector simulation. Even with this difference, the γ energy resolutions measured using the full ILD simulation when using the silicon and scintillator ECal options are similar. At very high energies, ≈ 500 GeV, the ECal is no longer sufficient to fully contain the γ s and so leakage into the HCal leads to a small degradation the energy resolution for the full simulation. This accounts for the deviation in the energy resolution between the full ILD simulation and the test beam parameterisation for the silicon ECal option.

Similarly, the energy resolution using test beam was parameterised as $\frac{57.6}{\sqrt{E_{Reco}}} \oplus 1.6\%$ for the nominal ILD HCal [2]. A comparison between this test beam parameterisation and the full ILD simulation, using the silicon ECal option, is shown in figure 2.4c. The test beam used for this parameterisation used π^\pm s with energies ranging from 10 to 80 GeV. In the determination of the test beam parameterisation, only showers starting in the HCal were considered whereas all showers were considered in the full ILD simulation. Negating showers starting in the ECal removes the effect of errors associated with the calibration of ECal for hadronic energy measurements and leads to a better energy resolution for the K_L^0 . The deviation between the test beam parameterisation and the full simulation grows at high K_L^0 energies due to the treatment of energy deposits leaking out of the back of the HCal. A tail catcher was used in the test beam analysis that had a similar structure to the HCal, but with a much wider average absorber thickness. Energy deposits in this tail catcher were calibrated in a similar fashion to the HCal giving a very good energy resolution for these energy deposits. In the full ILD simulation a muon chamber acts as the tail catcher, however, the calibration applied to energy deposits here is far less advanced than that applied to the test beam data meaning the energy resolution for these hits will be worse. Furthermore, energy deposits in the uninstrumented solenoid region of the full ILD simulation are not accounted for. These lost energy deposits and simplistic

calibration are the main causes of the deviation of the test beam parameterisation and the full simulation energy resolution for high energy K_L^0 s.

Combining these results together it is possible to demonstrate the effectiveness of particle flow calorimetry on the jet energy resolutions. After the decay of short lived particles approximately 60% of the energy of a jet is carried in the form of charged particles, 30% in the form of γ s and 10% in the form of neutral hadrons. A negligible amount of energy is also carried in the form of invisible energy i.e. neutrinos. In the traditional calorimetric approach the γ s are measured largely within the ECal, with an energy resolution of $\approx 0.15 \times \sqrt{E_\gamma}$, and the remaining particles are measured in the HCal, with an energy resolution of $\approx 0.55 \times \sqrt{E_h}$. Note here that these are the raw, not fractional energy resolutions. Therefore, the contributions to the fractional jet energy resolution are $\frac{0.08}{\sqrt{E_j}}$ from γ s and $\frac{0.46}{\sqrt{E_j}}$ from other particles where E_j is the jet energy. These add in quadrature to give a total jet energy resolution of $\frac{0.47}{\sqrt{E_j}}$. In the particle flow paradigm the energy of charged particles is measured in the tracker, which has such a good energy resolution that the contribution to the jet energy resolution is negligible. This means the contributions to the jet energy resolutions only come from γ s, $\frac{0.08}{\sqrt{E_j}}$, and from neutral hadrons, $\frac{0.17}{\sqrt{E_j}}$. When added in quadrature they give a total jet energy resolution of $\frac{0.19}{\sqrt{E_j}}$, which is significantly better than when using the traditional calorimetric approach. It must be emphasised that this is an upper limit on the performance as the effect of confusion will degrade the jet energy resolution. However, by applying sophisticated pattern recognition algorithms this confusion can be minimised and exceptional performance achieved.

The jet energy resolutions as a function of jet energy using the full ILD simulation are shown in figure 2.4d. Alongside this the intrinsic energy resolution and confusion contributions to the jet energy resolution are also presented. For low jet energies the jet energy resolution is dominated by the intrinsic energy resolution of the detector. This indicates that the charged particle track to calorimeter hit cluster associations being made are largely correct and that the resolution is being driven by the energy resolution of the calorimeters. For high jet energies the event topology is more dense and more error are present in the track cluster associations being made. Even at these large energies, the intrinsic energy resolution of the detector, which goes as $\frac{1}{\sqrt{E_j}}$, has reduced so much that the performance at high energies is better than that observed for the low energies. When the performance is put into context, these jet energy resolutions are sufficiently low, $\frac{\sigma_E}{E} \lesssim 3.8\%$ [1,7,12], that it is possible to separate

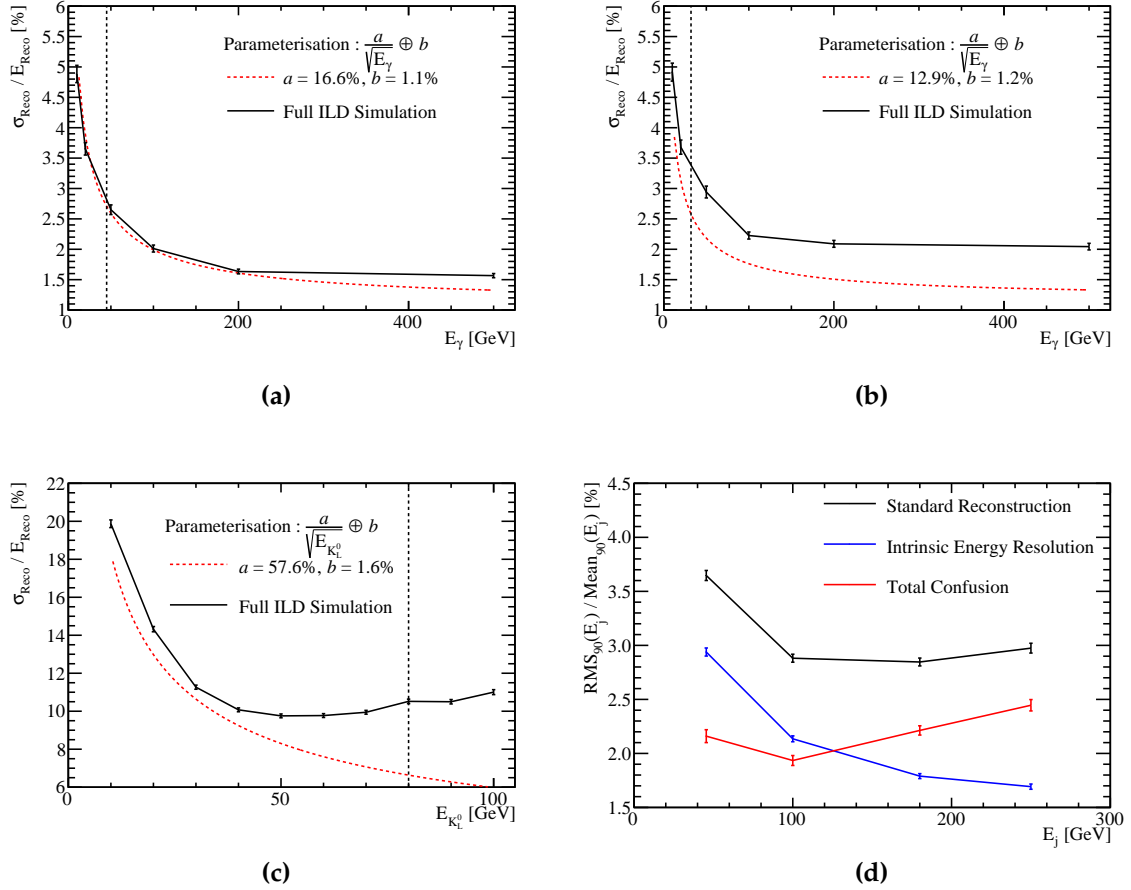


Figure 2.4: (a) The energy resolution as a function of γ energy using the nominal ILD model for the silicon ECal option. (b) The energy resolution as a function of γ energy using the nominal ILD model for the scintillator ECal option. (c) The energy resolution as a function of K_L^0 energy using the nominal ILD model with the silicon ECal option. (d) The jet energy resolution (RMS_{90}) as a function of jet energy using the nominal ILD model with the silicon ECal option. The intrinsic energy resolution and confusion contributions these the jet energy resolutions are also presented. The black dotted line on the single particle energy resolutions shows the highest energy particles used in the test beam measurements.

hadronic W and Z the hadronic decays, which is one of the key requirements for the future linear collider.

2.4 Electromagnetic Calorimeter Optimisation

The ECal primarily measures the energy deposits of electromagnetic showers. The default ILD detector model ECal, summarised in table 2.1, contains 24 radiation lengths (X_0 , which acts to confine all but the highest energy electromagnetic showers within it. The longitudinal structure of this default model is 29 readout layers, consisting of pairs of active and absorber material, and one presampling layer, which exists to encourage shower development. Increasing the thickness of the absorber material part way into the detector reduces the number of readout channels and cost of the overall calorimeter while retaining a high sampling rate at the start of particle showers, which is crucial for the pattern recognition aspect of particle flow calorimetry.

Parameter	Default Value
Transverse Segmentation	$5 \times 5 \text{ mm}^2$ square cells
Number of Layers	29 Readout Layers, 1 Presampling Layers
Active Material Choice	Silicon or Scintillator
Active Material Thickness	0.5 mm (Silicon) or 2 mm (Scintillator)
Absorber Material Choice	Tungsten
Absorber Material Thickness	20 Layers of 2.1 mm followed by 9 Layers of 4.2 mm

Table 2.1: Nominal ILD detector model ECal configuration.

The parameters being optimised in this study are:

- Transverse segmentation or cell size. This is a vital aspect of the detector in the particle flow paradigm as smaller cell sizes give greater potential for being able to separate energy deposits from charged and neutral particles. This transverse segmentation should have little to no effect on the intrinsic energy resolution of the detector.
- Number of Layers or cell depth. This parameter dictates the intrinsic energy resolution of the detector as smaller cell depths mean more sampling is done of the particle shower and so, due to the Poissonian statistics governing the measurement of particle showers, the better the resolution.
- Active material choice. This is a choice between silicon or scintillator. As well as providing different intrinsic energy resolutions the readout mechanics of these

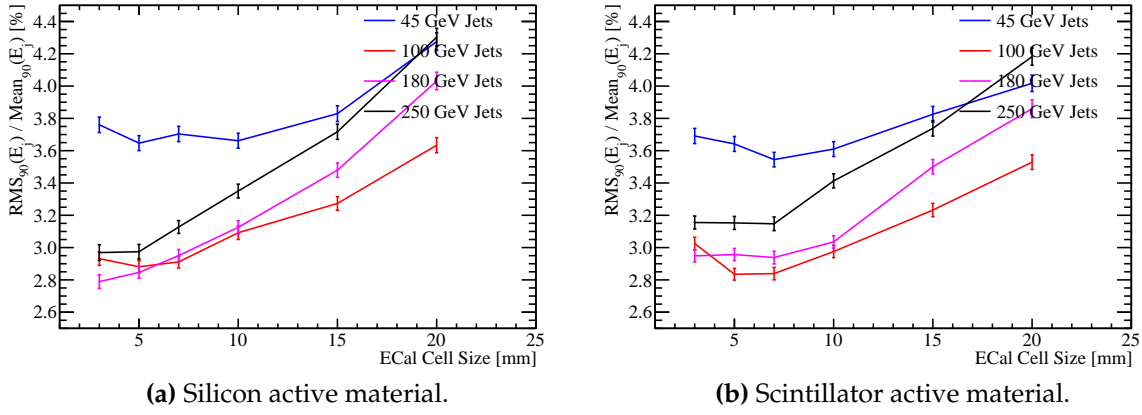


Figure 2.5: Jet energy resolution as a function of ECal cell size for the silicon and scintillator ECal options.

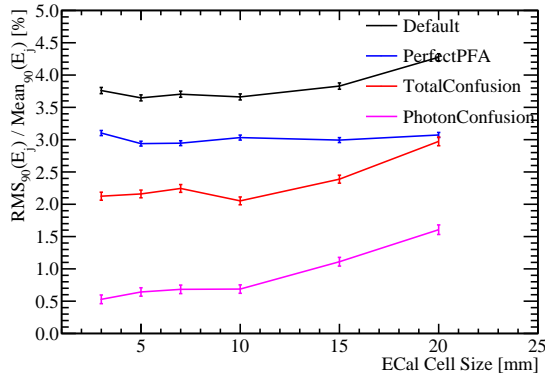
two options are significantly different. There is no clear prior knowledge as to which should provide better performance.

2.4.1 ECal Transverse Segmentation

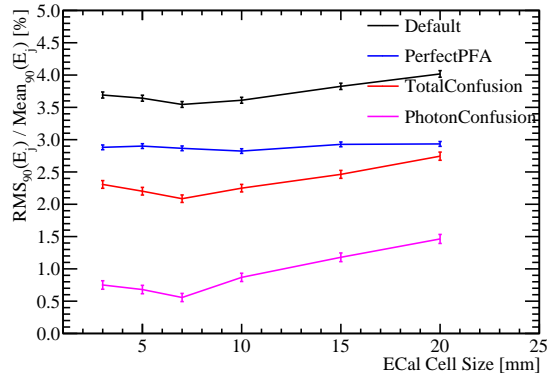
For this study a number of different detector models were considered where the transverse segmentation in the ECal had been varied about the nominal value of $5 \times 5 \text{ mm}^2$ square cells. The granularities considered were $3 \times 3 \text{ mm}^2$, $5 \times 5 \text{ mm}^2$, $7 \times 7 \text{ mm}^2$, $10 \times 10 \text{ mm}^2$, $15 \times 15 \text{ mm}^2$ and $20 \times 20 \text{ mm}^2$ square cells for both the silicon and scintillator active material options. The jet energy resolution as a function of transverse segmentation in the ECal is shown in figure 2.5.

The jet energy resolution was found to improve with decreasing cell size. This is expected as smaller cell size lead to better separation of energy deposits from neutral and charged particle showers.

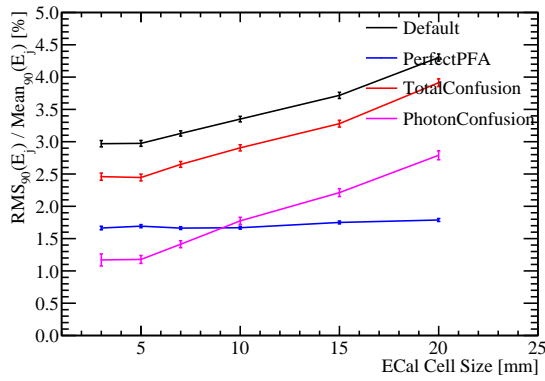
By examining the breakdown of the jet energy resolution into intrinsic resolution and confusion terms, as explained in chapter BLAH, it is possible to conclude that the dominant factor affecting the jet energy resolution when the transverse segmentation of the ECal is varied is the confusion arising from photon energy deposits. Examples of jet energy resolution breakdowns are shown for 45 and 250 GeV jets for both the silicon and scintillator ECal options in figure 2.6. As expected in the intrinsic energy resolution does not change significantly with the transverse segmentation.



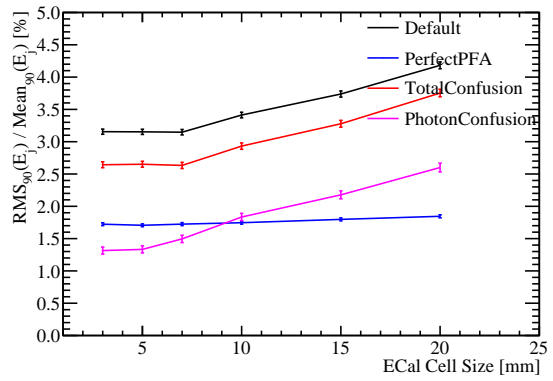
(a) Silicon active material, 45 GeV Jets.



(b) Scintillator active material, 45 GeV Jets.



(c) Silicon active material, 250 GeV Jets.



(d) Scintillator active material, 250 GeV Jets.

Figure 2.6: Jet energy resolution breakdown as a function of ECal transverse segmentation for 45 and 250 GeV jets. Results are given for both the silicon and scintillator ECal options.

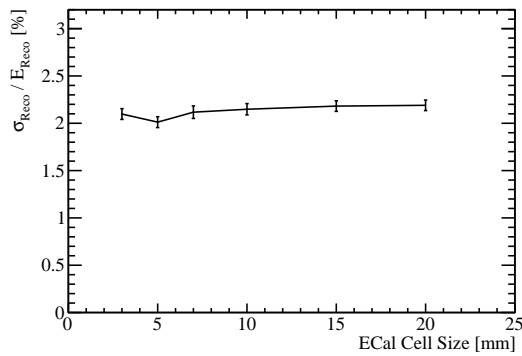
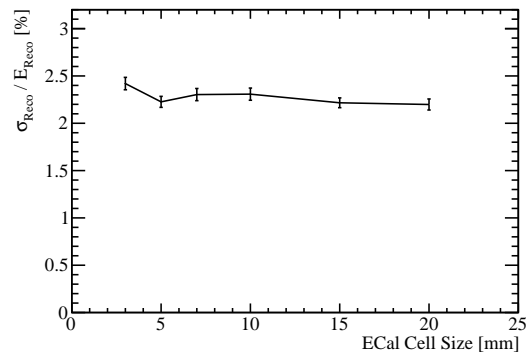
(a) Silicon active material, 100 GeV γ .(b) Scintillator active material, 100 GeV γ .

Figure 2.7: Energy resolution as a function of ECal transverse segmentation for 100 GeV photons. Results are given for both the silicon and scintillator ECal options.

A more targeted test of the intrinsic energy resolution of the ECal is presented in figure 2.7, which examines the energy resolution of single photon samples at 100 GeV. For the silicon option the intrinsic energy resolution was found to not vary significantly across the transverse granularities under consideration, however, there is a degradation in energy resolution with increasing cell size for the scintillator option. This originates from an inactive region of material in the simulation that represents the multi pixel photon counter (MPPC). The MPPC occupies a fixed area of the cell irrespective of cell size and so fractionally the "dead" region of the cell increases as cell size is reduced (cite this somehow). These trends will be present in the jet energy resolution studies, however, as only a small fraction, $\approx 10\%$, of the jet energy is measured in the ECal these trends will be washed out when looking purely at jets.

In conclusion smaller transverse granularities in the ECal significantly improve the jet energy resolution for both the silicon and scintillator options. The intrinsic energy resolution of the ECal is largely invariant to changes in the transverse segmentation for the silicon option, while larger transverse granularities are beneficial to the scintillator option as they reduce the impact of "dead" regions of the detector.

2.4.2 ECal Number of Layers

The performance of a number of detector configurations was examined where the number of layers of the ECal absorber material had been varied about the nominal value. This study was performed for both the silicon and scintillator active material options. In all cases considered tungsten was used as the absorber material in the ECal and the active layer thicknesses were not changed, that is 0.5 mm for the silicon option and 2 mm for the scintillator option. The layout of the ECal for detector models considered are summarised in table 2.2. For each detector model considered in this study the total number of radiation lengths in the ECal is kept approximately constant. This is done by varying the thickness of the absorber material when modifying the number of layers in the ECal.

The jet energy resolution was found to improve with increasing number of layers. This is expected as a more layers in the calorimeter, for the same total thickness, implies greater sampling of the particle shower and so, as the energy resolution obeys Poissonian statistics, an improvement in the intrinsic energy resolution is observed. A

Total Number of Layers $N_{\text{Layers ECal}}$	N_{Layers} Region 1	Absorber Thickness Region 1 [mm]	N_{Layers} Region 2	Absorber Thickness Region 2 [mm]	Total Thickness [X_0]
30	20	2.10	9	4.20	22.77
26	17	2.40	8	4.80	22.60
20	13	3.15	6	6.30	22.47
16	10	4.00	5	8.00	22.31

Table 2.2: Transverse segmentation layout of the ECal models considered. Radiation length of tungsten absorber is 3.504mm [10]. Note that the presampler layer contributes one layer to the cumulative number of layers value for all detector models considered.

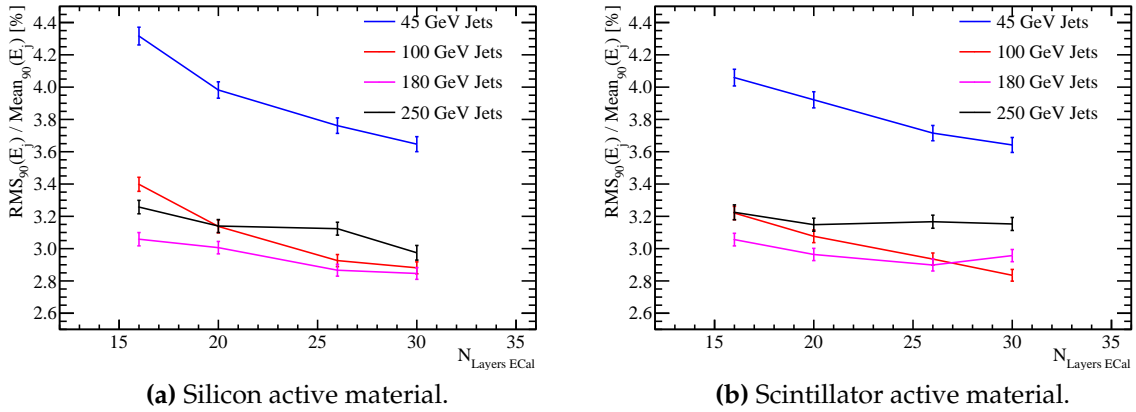
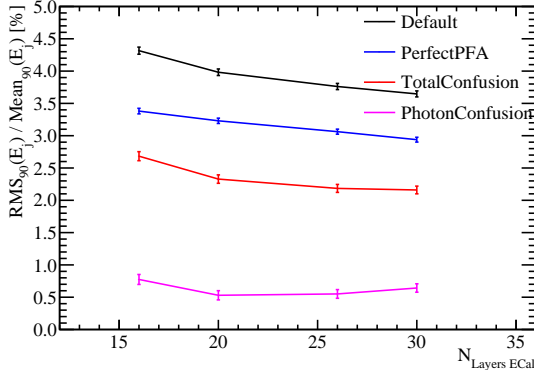


Figure 2.8: Jet energy resolution as a function of number of layers in the ECal for the silicon and scintillator ECal options.

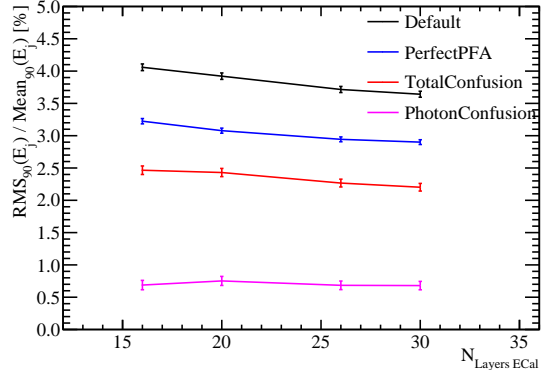
particularly strong dependency on ECal number of layers is noted at low energies, but this reduces significantly as energies rise.

The strong dependency of the jet energy resolution on the ECal number of layers can be expanded upon by looking at the decomposition of the jet energy resolution, which is shown in figure 2.9 for the 45 and 250 GeV energy jets. At low energies the trend is twofold: an improvement to the intrinsic energy resolution with more sampling of particle showers and a reduction in the impact of confusion. For high energy jets, where confusion dominates, there is little to no change in the intrinsic energy resolution and confusion as a function of ECal transverse segmentation.

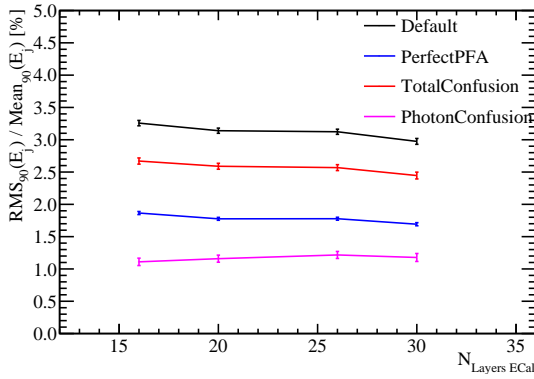
Further understanding is gained by considering the energy resolution of single photon samples at 100 GeV as a function of the number of layers in the ECal, which is



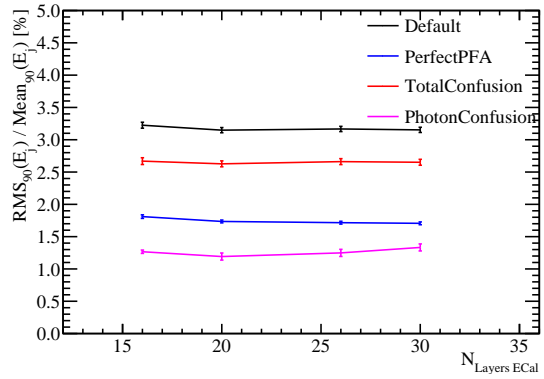
(a) Silicon active material, 45 GeV Jets.



(b) Scintillator active material, 45 GeV Jets.



(c) Silicon active material, 250 GeV Jets.



(d) Scintillator active material, 250 GeV Jets.

Figure 2.9: Jet energy resolution breakdown as a function of ECal number of layers for 45 and 250 GeV jets. Results are given for both the silicon and scintillator ECal options.

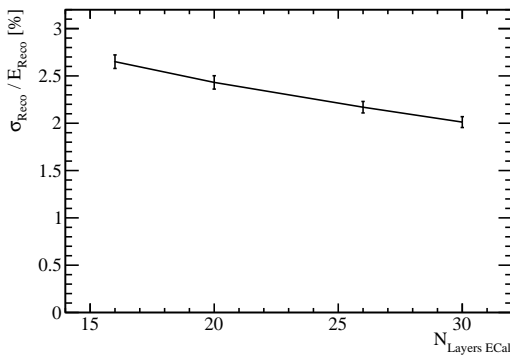
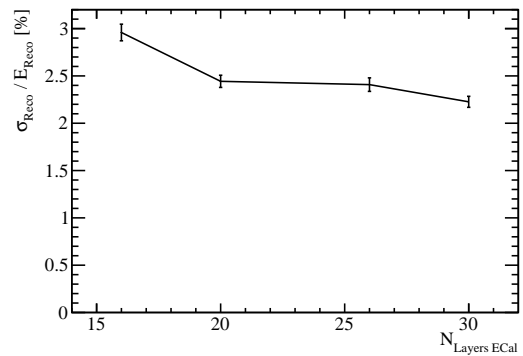
(a) Silicon active material, 100 GeV γ .(b) Scintillator active material, 100 GeV γ .

Figure 2.10: Energy resolution as a function of function of ECal number of layers for 100 GeV photons. Results are given for both the silicon and scintillator ECal options.

shown in figure 2.10. At these large photon energies it is clear that the intrinsic energy resolution of the ECal is improved by having finer longitudinal segmentation in the ECal. This trend will be present in the jet energy resolution study, but as only $\approx 10\%$ of the jet energy is measured in the ECal in comparison to $\approx 100\%$ of the photons energy, it will be obscured by the energy resolution of the rest of the detector, which is invariant to the ECal longitudinal segmentation.

The intrinsic energy resolution of the ECal is improved by having a finer transverse segmentation. This is evident when looking at the energy resolution of photons whose energy deposits are localised within the ECal. This trend is again clear when considering the energy resolution of low energy jets, however, at higher energies the number of layers in the ECal is not a significant factor in determining detector performance.

2.4.3 ECal Active Material

In sections 2.4.1 and 2.4.2 the performance of the ECal was reported for both the silicon and scintillator options and to a large extent the performance of the two options was the same. There were a few differences, which attention should be brought to:

- The intrinsic energy resolution of a silicon ECal is worse than that of a scintillator ECal for low energies, while the trend is reversed at high energies. The cross over point in performance occurs between 20 and 50 GeV. This trend is shown in figure ??.
- The "dead" region due to the presence of the MPPC in the scintillator option degrades performance of the detector for small transverse granularities. No such effect is seen for the silicon option. This effect is shown in figure 2.7.

The lack of this "dead" region of the detector and the beneficial intrinsic energy resolution at large energies indicates a preference for a silicon detector, however, there is no clear preference based on these studies.

2.5 Hadronic Calorimeter Optimisation

The HCal is designed to measure the energy deposits from hadrons. The default ILD detector model HCal, summarised in table 2.3, contains ≈ 6 nuclear interaction lengths (λ_I). The ECal contributes approximately one λ_I giving a total of $\approx 7\lambda_I$, which is sufficient to confine the bulk of jets up to 1 TeV events, which is the maximum running energy for the ILC. The longitudinal structure of this model consists of 48 readout layers each containing a 3 mm active layer of scintillator and a 20 mm absorber layer of iron. There are several readout technology options under consideration for the HCal, which are analogue, digital and semi-digital, however, for this study only the analogue HCal is considered.

Parameter	Default Value
Transverse Segmentation	$30 \times 30\text{mm}^2$ square cells
Number of Layers	48 Readout Layers
Active Material Choice	Scintillator Tiles
Active Material Thickness	3 mm
Absorber Material Choice	Steel
Absorber Material Thickness	20 mm

Table 2.3: Nominal ILD detector model HCal configuration.

The parameters being optimised in this study are:

- Transverse segmentation or cell size. This is key to successful application of pattern recognition in the particle flow paradigm, but should not change intrinsic energy resolution.
- Number of Layers or cell depth. This governs the intrinsic energy resolution of a calorimeter.
- Depth of calorimeter. This is important in determining the impact of leakage of energy out of the detector.
- Sampling fraction. This is the ratio of the active medium thickness to the absorber medium thickness. As sampling calorimetry is based on sampling of particle showers it is expected that this is an important parameter. However, above a given sampling fraction there should be little difference between performance if

showers are sampled at a high enough rate to get a good estimate of the incoming particles energy.

- Absorber material choice. This is a choice between steel or tungsten. While this does not change the active medium choice it does dictate the growth and propagation of showers and so plays a crucial role in calorimetry. While tungsten is more expensive than steel for the raw material the larger number of interaction lengths per length scale for tungsten mean that it is possible to create a smaller detector with the same number of interaction lengths within it. This reduces the size of the solenoid needed to generate the magnetic field and so lowers the price of the detector. As both of these materials are viable as absorber medium choices it is crucial to determine if either is more advantageous from a physics perspective.

2.5.1 HCal Absorber Material

The nominal choice of absorber material is steel, tungsten provides a feasible alternative material. While more expensive than steel, tungsten contains more radiation lengths per unit length than steel and so the overall size of the detector would reduce meaning the solenoid could be smaller, which would to first order offset the additional cost of the tungsten. This section aims to determine whether either of these options is beneficial when considering the jet energy resolution of the detector.

In this study the total depth of absorber material, in nuclear interaction lengths, was held constant for both models. This was to ensure any performance changes were not due to additional material as opposed to the intrinsic energy resolutions of the absorber materials. The interaction of hadrons with the absorber material within the detector is simulated by GEANT4. The model for these interactions is dependent upon the choice of physics list, which by default is the QGSP_BERT physics list. This list is recommended by the GEANT4 authors to use for high energy physics calorimetry as it gives good agreement between experiment. For this study both the QGSP_BERT and the QGSP_BERT_HP physics lists are tested. The QGSP_BERT_HP list uses the high precision neutron package (NeutronHP) to deal with the transportation of neutrons from below 20 MeV to thermal energies. This added detail was thought to be necessary for a study involving tungsten due to the increased time of shower development.

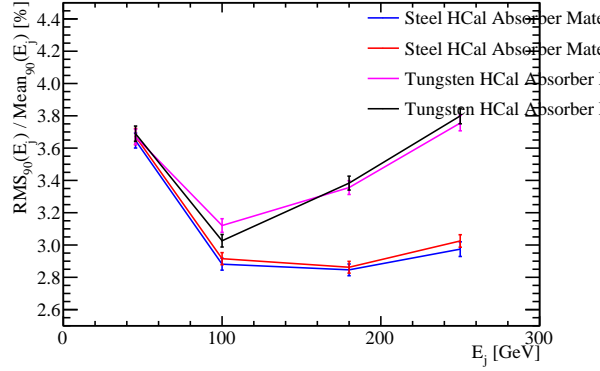


Figure 2.11: Jet energy resolution as a function of jet energy for various absorber materials in the HCal and physics lists.

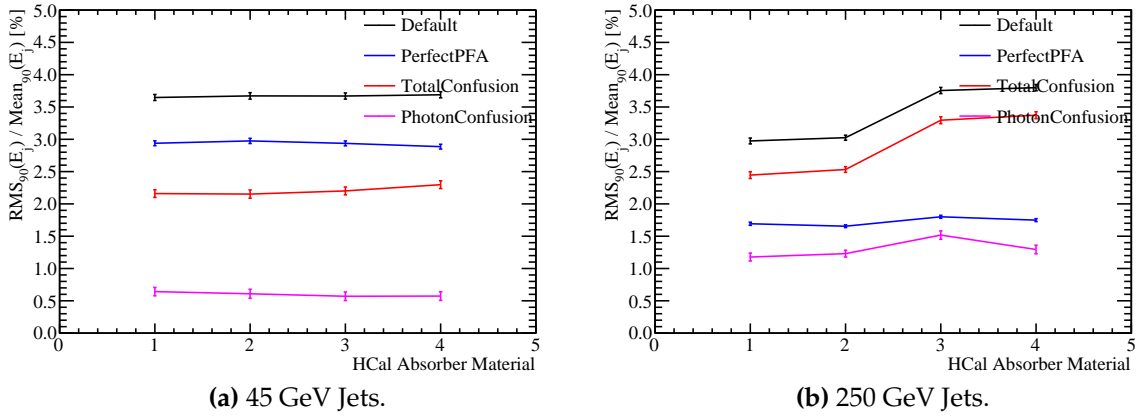


Figure 2.12: Jet energy resolution breakdown as a function of HCal absorber material and physics list for 45 and 250 GeV jets.

The jet energy resolution for the steel and the tungsten HCal options, for using both the QGSP_BERT and the QGSP_BERT_HP physics lists, are shown in figure 2.11 as a function of jet energy. These results indicate that steel outperforms tungsten as an absorber material, particularly for high energy jets. At low energies the performance is similar, indicating that the intrinsic energy resolution of the two options is comparable. The use of the QGSP_BERT_HP physics list, as opposed to QGSP_BERT, has a minimal impact on these results.

Expanding upon this further by examining the jet energy resolution breakdowns as shown in figure 2.12, it can be seen that the change in performance when changing the HCal absorber material from steel to tungsten is due to changes in the confusion. The change in confusion is most likely due to the fact that the PandoraPFA algorithms

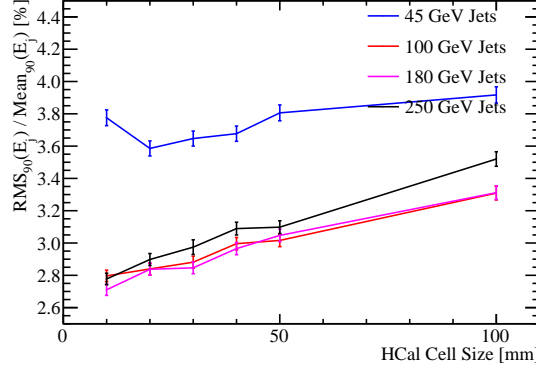


Figure 2.13: Jet energy resolution as a function of HCal cell size.

are tuned for HCal cell dimensions based on the steel HCal option, while the HCal cells for the tungsten option HCal will be smaller by a factor of approximately 1.7 ($\approx 16.77/9.946$). The jet energy resolution breakdowns also indicate that the intrinsic energy resolution of the tungsten HCal is marginally worse, particularly for high energy jets, than that of a steel HCal.

In conclusion, the steel option HCal outperforms the tungsten option in terms of intrinsic energy resolution and pattern recognition confusion making it the more preferred option of the two.

2.5.2 HCal Transverse Segmentation

For this study a number of different detector models were considered where the transverse segmentation in the HCal had been varied about the nominal value of $30 \times 30 \text{ mm}^2$ square cells. The granularities considered were $10 \times 10 \text{ mm}^2$, $20 \times 20 \text{ mm}^2$, $30 \times 30 \text{ mm}^2$, $40 \times 40 \text{ mm}^2$, $50 \times 50 \text{ mm}^2$ and $100 \times 100 \text{ mm}^2$ square cells. The jet energy resolution as a function of transverse segmentation in the HCal is shown in figure 2.13.

As with the case for the ECal, the jet energy resolution was found to improve with decreasing cell size as smaller cell size lead to better separation of energy deposits from neutral and charged particle showers.

The jet energy resolution breakdowns, shown in figure, 2.14, show that the confusion term varies when changing the HCal transverse segmentation, but the intrinsic energy resolution does not. Furthermore, the photon confusion is invariant to changes in HCal transverse segmentation, indicating that the observed overall performance

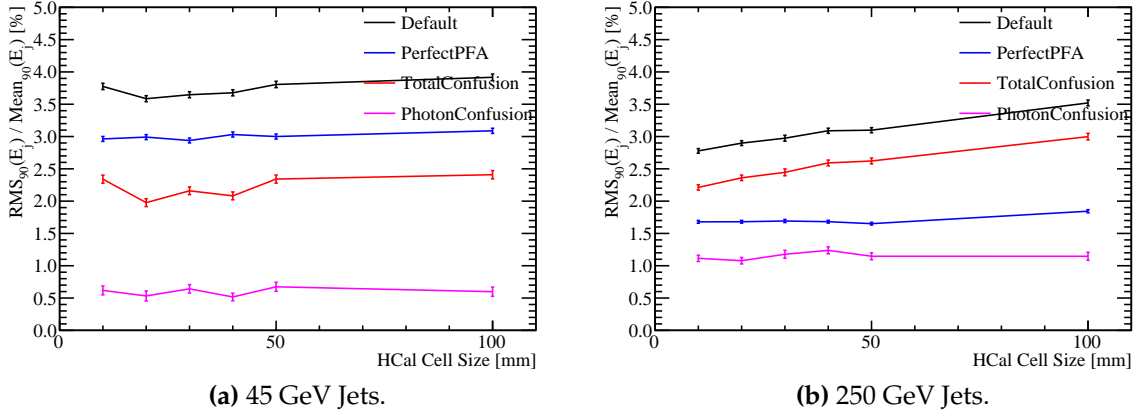


Figure 2.14: Jet energy resolution breakdown as a function of HCal transverse segmentation for 45 and 250 GeV jets.

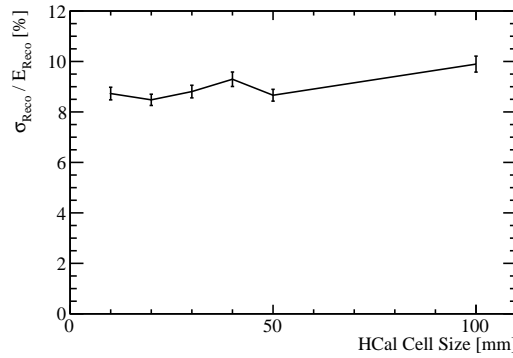


Figure 2.15: Energy resolution as a function of HCal transverse segmentation for 50 GeV K_L^0 .

changes are due to the effects of confusion arising from energy deposits from charged and neutral hadrons. Once again for 45 GeV jets the detector performance is dominated by intrinsic energy resolution and so HCal transverse segmentation has little effect, while for 250 GeV jets the performance is dominated by confusion and HCal transverse segmentation becomes more significant.

The energy resolution of single long lived neutral kaons, K_L^0 , at 50 GeV is considered as a function of transverse segmentation in the HCal. This is shown in figure 2.15 and, as expected, the energy resolution of the detector is largely invariant to changes in the transverse segmentation in the HCal. As these K_L^0 samples may deposit energy in the ECal, this figure represents the intrinsic energy resolution of the ILD detector as a whole and not purely that of the HCal. However, it is expected that the bulk of the

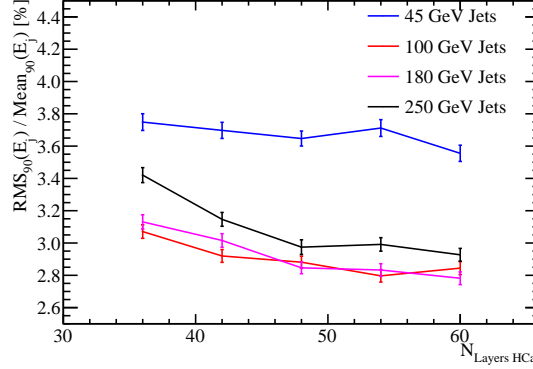


Figure 2.16: Jet energy resolution as a function of number of layers in the HCal.

energy deposited by these samples occurs within the HCal and so such plots are a useful representation of the HCal performance.

The transverse segmentation of the HCal acts to determine the impact of confusion from charged and neutral hadron energy deposits. It does not vary the intrinsic energy resolution of the detector, nor does it impact the reconstruction of photons. As confusion is dominant at high jet energies the HCal transverse segmentation gains an increasing role in determining detector performance as the energy in an event increases.

2.5.3 HCal Number of Layers

This section focuses upon change in detector performance when varying the number of layers in the HCal. For this study, the absorber and active layer thicknesses are not varied when adding or subtracting layers from the HCal, so both the total depth of the HCal as well as the number of sampling points of the hadronic showers varies simultaneously, this is in comparison to the study described in section 2.5.5 where the total depth of the HCal is fixed. The detector models considered had 36, 42, 48, 54 and 60 layered HCal.

The jet energy resolution for the various detector models considered is shown in figure 2.22. It was found that increasing the number of layers in the HCal improved the jet energy resolution for high energy jets, while for low energy jets no the performance change was observed. The breakdown of the jet energy resolution for the high energy

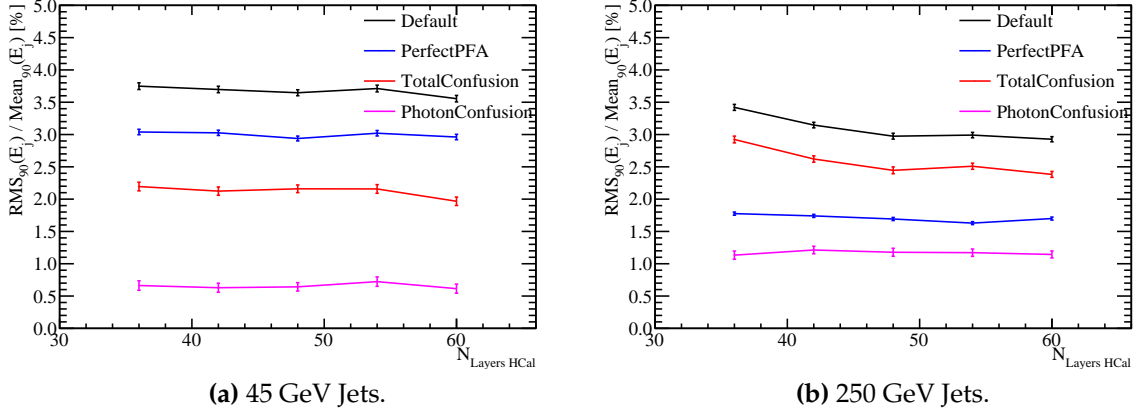


Figure 2.17: Jet energy resolution breakdown as a function of number of layers in the HCal for 45 and 250 GeV jets.

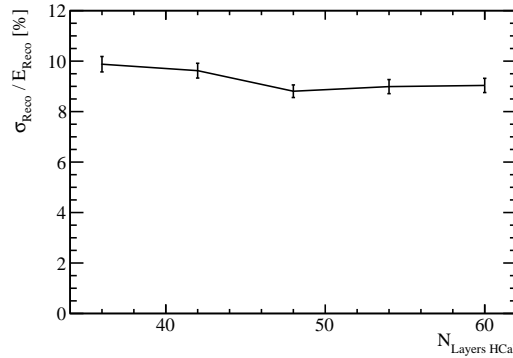


Figure 2.18: Energy resolution as a function of number of layers in the HCal for 50 GeV K_L^0 .

jets, shown in figure ??, indicates a reduction in the confusion term is driving the change in performance when increasing the number of layers in the HCal.

While the intrinsic energy resolution for jets appeared largely invariant to changes in the number of layers in the HCal, it can be seen that there is an associated improvement in the energy resolution for neutral hadrons, which can be seen in figure 2.18. This change in neutral hadron energy resolution will be masked in the jet energy resolution study as only $\approx 10\%$ of the energy of a jet is carried in the form of neutral hadrons and the energy resolution change is minimal.

In conclusion, a larger number of layers in the HCal is beneficial to detector performance both in terms of a reduction in pattern recognition confusion as well as an improvement in the energy resolution of neutral hadrons. These performance changes

at the energies considered are relatively small and so it would be feasible to consider changes to the nominal number of HCal layers. However, at higher energies these conclusions could be significantly modified as leakage dominates.

2.5.4 HCal Sampling Fraction

In this section the sampling fraction, the ratio of the active to absorber layer thicknesses were considered. For all detector models considered in this section the total number of nuclear interaction lengths in the HCal was held constant, as was the number of layers in the HCal and the transverse segmentation. The detector models considered are summarised in table 2.4.

Sampling Fraction	Absorber Thickness [mm]	Active Thickness [mm]
0.05	20.430	1.022
0.10	20.213	2.021
0.15	20.000	3.000
0.20	19.792	3.958
0.25	19.587	4.897

Table 2.4: Sampling fraction of HCal models considered.

The jet energy resolution for these detector models is shown in figure 2.22. It was found that there is no significant change in performance when varying the sampling fraction.

2.5.5 HCal Sampling Frequency

This section aims to determine the change in performance when the sampling frequency, the number of times a particle shower is sampled per unit length, in the HCal is varied. This was done by varying the number of readout layers, while maintaining the total number of nuclear interaction lengths contained within the HCal. In all cases the absorber material was steel while the active material was scintillator. Each HCal configuration had the same total number of nuclear interaction lengths, $5.72 \lambda_I$ in the absorber material and $0.19 \lambda_I$ in the active material, however, the thickness of the

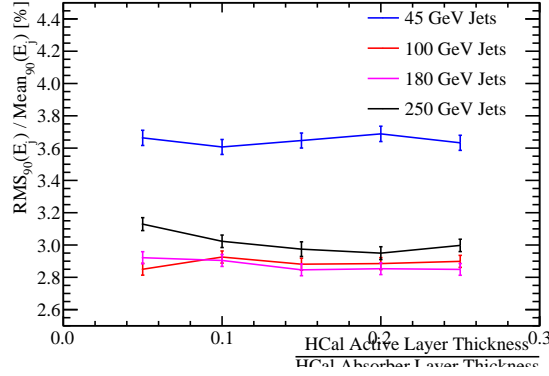


Figure 2.19: Jet energy resolution as a function of sampling frequency in the HCal. Label needs fixing.

layers was varied depending on the total number of layers being considered. The ratio of the active material layers to the absorber material layers, the sampling fraction, was also kept constant in this study. A summary of the detector models considered in this study can be found in table 2.5.

Number $N_{\text{Layers HCal}}$	Absorber Thickness [mm]	Active Thickness [mm]
60	16.00	2.40
54	17.78	2.67
48	20.00	3.00
42	22.86	3.43
36	26.67	4.00
30	32.00	4.80
24	40.00	6.00
18	53.33	8.00

Table 2.5: Transverse segmentation layout of various HCal models considered.

The jet energy resolution for the various detector models considered is shown in figure 2.22. It was found that increasing the number of layers in the HCal, for the same total thickness, improved the jet energy resolution for all jet energies considered. Based on the increase in the frequency of sampling of particle showers in the HCal, it is expected that the intrinsic energy resolution of the detector should improve. However,

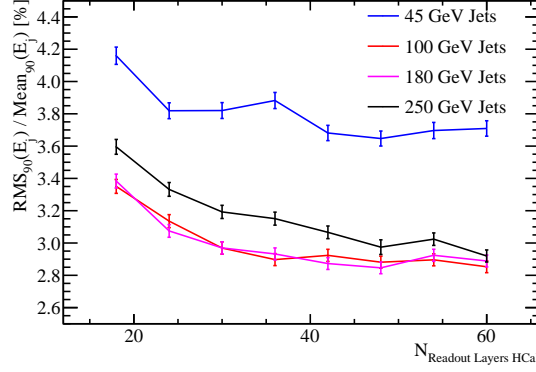


Figure 2.20: Jet energy resolution as a function of sampling frequency in the HCal.

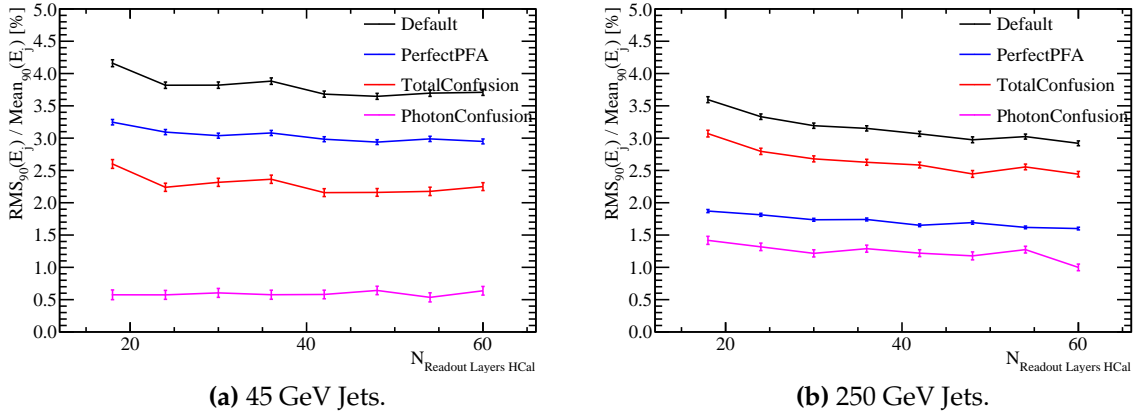


Figure 2.21: Jet energy resolution breakdown as a function of HCal sampling frequency for 45 and 250 GeV jets.

the improvement observed in jet energy resolution for high energy jets indicates that sampling frequency is also affecting the confusion terms.

These trends are further explored by considering the breakdown of jet energy resolution, which are shown in figure 2.21. As expected from the standard performance reconstruction trends as a function of jet energy, there is an improvement in both the intrinsic energy resolution and a reduction in the impact of confusion when the number of layers in the HCal is increased. The dominant trend driving the overall detector performance is that associated with the confusion of separating energy deposits from charged and neutral particles. This emphasises the importance of pattern recognition to detector performance in the particle flow paradigm.

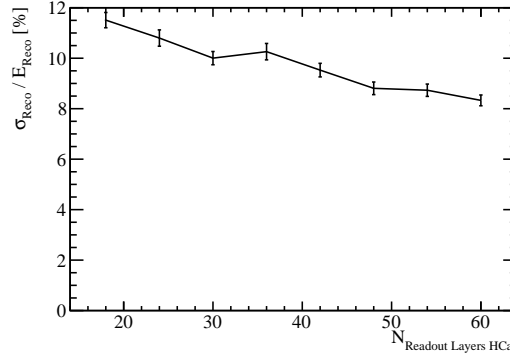


Figure 2.22: Energy resolution as a function of HCal sampling frequency for 50 GeV K_L^0 .

The change in the intrinsic energy resolution of the HCal when varying the sampling frequency is best summarised by looking at the energy resolution of neutral hadrons. A plot of energy resolution against the number of readout layers in the HCal for 50 GeV K_L^0 can be found in figure 2.22. This data shows that a reduction in sampling frequency of a particle shower that accompanies a reduction in the number of readout layers results in a broadening of energy distributions and a degradation in the resolution. It should again be emphasised that these results are for the full ILD detector model and so include the effect of the $\approx 1\lambda_I$ in the ECal.

The increasing the HCal sampling frequency has a twofold effect on the detector performance: an increase in sampling rate of particle showers and an improvement to the intrinsic energy resolution and a reduction in the confusion arising from associating energy deposits from hadrons.

2.6 Global Detector Parameters

This section focuses upon optimisation of two global detector parameters; the magnetic field strength and the ECal inner radius. While these are not directly related to the calorimeter they will both effect detector performance and so were deemed worthy of study alongside the calorimeter parameters.

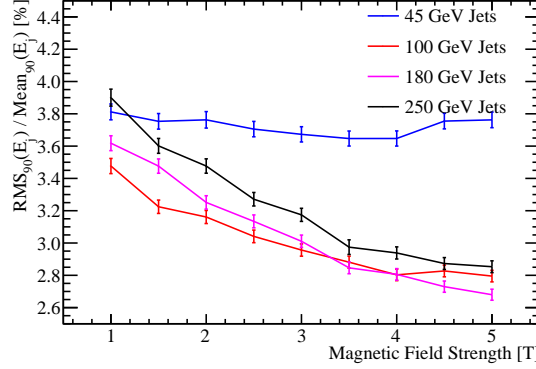


Figure 2.23: Jet energy resolution is shown for several fixed energy jets as a function of magnetic field strength.

2.6.1 The Magnetic Field Strength

The magnetic field is vital to the successful application of particle flow calorimetry. Any charged particles passing through the detector transverse helices that, once reconstructed, can be fitted to give the momentum and so energy of said particle in the particle flow paradigm. The magnetic field also created a separation between charged and neutral hadrons energy deposits in the calorimeters. The larger the magnetic field, the greater this separation and the easier to avoid confusion associate tracks to the correct energy deposits in the calorimeters, which is crucial for particle flow.

The magnetic field strengths considered in this study ranged from 1 to 5 T in steps of 0.5 T. The jet energy resolutions as a function of magnetic field strength, shown in figure 2.23, shows that the jet energy resolution decreases with increasing magnetic field strength for high energy jets. At low energies the performance is largely invariant to magnetic field strength.

Examination of the decompositions of the jet energy resolution, found in figure 2.24, highlights a number of effects.

The first is a clear reduction in confusion with increasing magnetic field strength. This is due to a larger separation between charged and neutral hadron energy deposits in the calorimeter as was expected.

Secondly there is a reduction in intrinsic energy resolution with increasing magnetic field strength for low energy jets, while for high energy jets this trend is reversed. At low energies the momenta of the charged particles will be low and so the radii

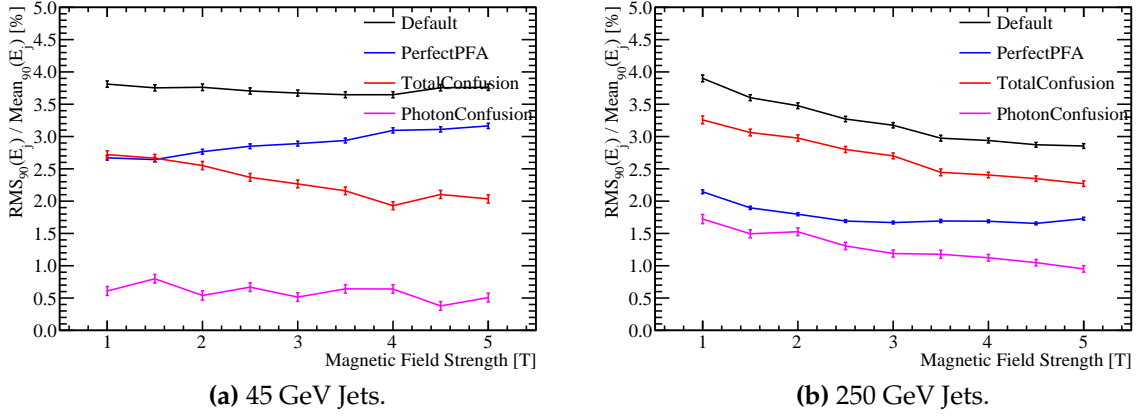


Figure 2.24: Jet energy resolution breakdown as a function of magnetic field strength for 45 and 250 GeV jets.

of curvature of the helix these particles transverse will be small. If the radius for a given particle is small enough it will not make it into the calorimeters. In this case only if the track produced from this particle passes tight selection cuts designed to ensure the track originates from the impact point will the track be used to create a PFO. Therefore, energy can and will be lost in from events where PFOs are stuck within the tracker. Given the radii of curvature is inversely proportional to the magnetic field strength, the larger the magnetic field strength the more tracks will be confined to the tracker. The more tracks that are confined to the tracker, the worse the intrinsic energy resolution becomes as inevitably some tracks fail the quality cuts to form PFOs. At high jet energies the transverse momentum of the particles will be sufficiently large that the radii of curvatures of the helices formed by charged particles will be enough so that they reach the calorimeters on average. However, for low magnetic field strengths more particles deposit energy within the same calorimeter cells. The intrinsic energy resolution plot is determined by associating a single MC particle to each calorimeter cell. At high jet energies and low magnetic field strengths many of the cells will have energy deposits split between multiple cells and so associating a single MC particle per cell is inaccurate. This explains why the intrinsic energy resolution degrades slightly in this scenario. These results are still of interest, however, because the driving term in the jet energy resolution as a function of magnetic field strength is the confusion.

In summary, increasing the magnetic field strength is beneficial to detector performance as it reduces confusion from associating tracks to calorimetric energy deposits from charged particles. While there is a reduction in the intrinsic energy resolution

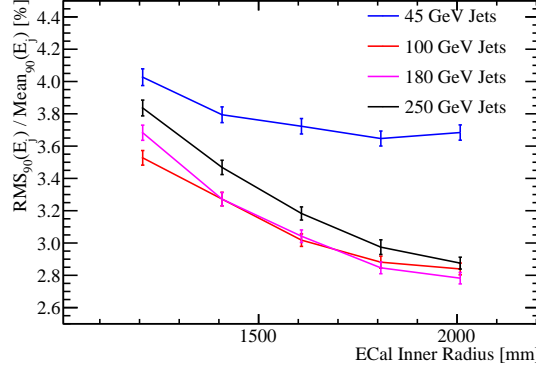


Figure 2.25: Jet energy resolution is shown for several fixed energy jets as a function of ECal inner radius.

for low transverse momentum jets with increasing magnetic field strength, this effect is largely offset by the change in confusion. While the nominal field of 3.5 T gives good performance increasing the field strength is a clear way of making large gains in detector performance.

2.6.2 Inner ECal Radius

This section focuses on optimising the inner ECal radius, or the outer tracker radius. The nominal detector model has an ECal inner radius of 1808 mm and for this optimisation detector models were considered where the ECal inner radii was set to 1208, 1408, 1608 and 2008 mm. All other detector parameters identical to those of the nominal ILD detector model.

The jet energy resolution as a function of ECal inner radius is shown in figure 2.25 and these results show that a large ECal inner radius was highly beneficial to detector performance. This is due to the fact that a large tracker gives more time for charged particles to bend due to the magnetic field, which creates a larger separation between calorimetric energy deposits from charged and neutral particles. This larger separation reduces the confusion when associating calorimetric energy deposits to tracks and so improves the detector performance. This conclusion is backed up by the decomposition of the jet energy resolution for the low and high energy jets, shown in figure ??, which explicitly show a reduction in confusion with increasing ECal inner radius.

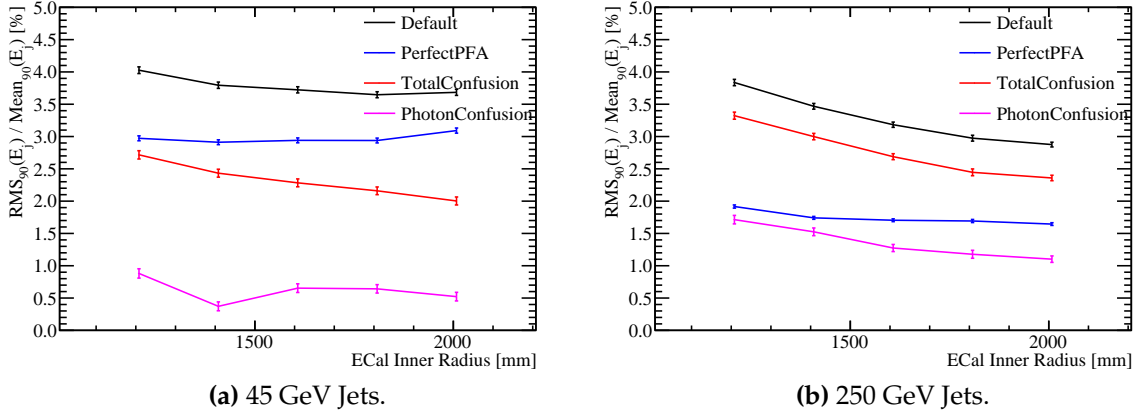


Figure 2.26: Jet energy resolution breakdown as a function of ECal inner radius for 45 and 250 GeV jets.

The intrinsic energy resolution of the detectors follows the same pattern as was observed in the magnetic field study. For low energy jets the larger ECal radius means fewer particles make it to the calorimeters and so some PFOs are not reconstructed giving a worse energy resolution. While at larger jet energies the radii of curvature of the charged particles is sufficiently large as the particles have higher momenta, meaning very few are confined to the tracker and so the intrinsic energy resolution is largely invariant. There is a small degradation in intrinsic energy resolution at low ECal inner radii due to the association of a single MC particle per calorimeter cell when running the cheated pattern recognition as explained in section 2.6.1. Again, this effect has little bearing on the final conclusions as the change in intrinsic energy resolution across the detector models is a second order effect.

In conclusion, increasing the ECal inner radius benefits the jet energy resolution significantly. This trend is driven by changes to the confusion in associating tracks to calorimetric energy deposits, with a larger ECal inner radius producing a reduction in the confusion as separation of charged and neutral particle energy deposits increases.

2.7 Conclusions

Colophon

This thesis was made in $\text{\LaTeX}2_\epsilon$ using the “hepthesis” class [\[5\]](#).

Bibliography

- [1] Halina Abramowicz et al. The International Linear Collider Technical Design Report - Volume 4: Detectors. 2013, 1306.6329.
- [2] C. Adloff et al. Hadronic energy resolution of a highly granular scintillator-steel hadron calorimeter using software compensation techniques. *JINST*, 7:P09017, 2012, 1207.4210.
- [3] S. Agostinelli et al. GEANT4: A Simulation toolkit. *Nucl. Instrum. Meth.*, A506:250–303, 2003.
- [4] G. Alexander et al. A Comparison of b and (uds) quark jets to gluon jets. *Z. Phys.*, C69:543–560, 1996.
- [5] Andy Buckley. The hepthesis L^AT_EX class.
- [6] F. Gaede. Marlin and LCCD: Software tools for the ILC. *Nucl. Instrum. Meth.*, A559:177–180, 2006.
- [7] Lucie Linssen, Akiya Miyamoto, Marcel Stanitzki, and Harry Weerts. Physics and Detectors at CLIC: CLIC Conceptual Design Report. 2012, 1202.5940.
- [8] J. S. Marshall, A. Mäijnnich, and M. A. Thomson. Performance of Particle Flow Calorimetry at CLIC. *Nucl. Instrum. Meth.*, A700:153–162, 2013, 1209.4039.
- [9] P. Mora de Freitas and H. Videau. Detector simulation with MOKKA / GEANT4: Present and future. In *Linear colliders. Proceedings, International Workshop on physics and experiments with future electron-positron linear colliders, LCWS 2002, Seogwipo, Jeju Island, Korea, August 26-30, 2002*, pages 623–627, 2002.
- [10] C. Patrignani et al. Review of Particle Physics. *Chin. Phys.*, C40(10):100001, 2016.
- [11] Torbjorn Sjostrand, Stephen Mrenna, and Peter Z. Skands. PYTHIA 6.4 Physics and Manual. *JHEP*, 05:026, 2006, hep-ph/0603175.

- [12] M. A. Thomson. Particle Flow Calorimetry and the PandoraPFA Algorithm. *Nucl. Instrum. Meth.*, A611:25–40, 2009, 0907.3577.

List of figures

2.1	500 GeV di-jet $Z \rightarrow uds$ event display for nominal ILD detector.	5
2.2	Definition of jet energy resolution. Reconstructed jet energy for 200 GeV di-jet $Z \rightarrow uds$ events for nominal ILD detector.	6
2.3	The reconstructed energy distribution for (a) 50 GeV K_L^0 and (b) 100 GeV γ events. The red line shows a Gaussian fit used to parameterise the detector performance. The fit was applied to the truncated range of the reconstructed PFO energy distribution containing at least 75% of the data with the narrowest RMS. The nominal ILD model was used in this simulation.	8
2.4	(a) The energy resolution as a function of γ energy using the nominal ILD model for the silicon ECal option. (b) The energy resolution as a function of γ energy using the nominal ILD model for the scintillator ECal option. (c) The energy resolution as a function of K_L^0 energy using the nominal ILD model with the silicon ECal option. (d) The jet energy resolution (RMS_{90}) as a function of jet energy using the nominal ILD model with the silicon ECal option. The intrinsic energy resolution and confusion contributions these the jet energy resolutions are also presented. The black dotted line on the single particle energy resolutions shows the highest energy particles used in the test beam measurements.	12
2.5	Jet energy resolution as a function of ECal cell size.	14
2.6	Jet energy resolution breakdown as a function of ECal transverse segmentation for 45 and 250 GeV jets. Results are given for both the silicon and scintillator ECal options.	15

2.7	Energy resolution as a function of ECal transverse segmentation for 100 GeV photons. Results are given for both the silicon and scintillator ECal options.	15
2.8	Jet energy resolution as a function of number of layers in the ECal. . .	17
2.9	Jet energy resolution breakdown as a function of ECal number of layers for 45 and 250 GeV jets. Results are given for both the silicon and scintillator ECal options.	18
2.10	Energy resolution as a function of ECal number of layers for 100 GeV photons. Results are given for both the silicon and scintillator ECal options.	18
2.11	Jet energy resolution as a function of jet energy for various absorber materials in the HCal and physics lists.	22
2.12	Jet energy resolution breakdown as a function of HCal absorber material and physics list for 45 and 250 GeV jets.	22
2.13	Jet energy resolution as a function of HCal cell size.	23
2.14	Jet energy resolution breakdown as a function of HCal transverse segmentation for 45 and 250 GeV jets.	24
2.15	Energy resolution as a function of HCal transverse segmentation for 50 GeV K_L^0	24
2.16	Jet energy resolution as a function of number of layers in the HCal. . .	25
2.17	Jet energy resolution breakdown as a function of number of layers in the HCal for 45 and 250 GeV jets.	26
2.18	Energy resolution as a function of number of layers in the HCal for 50 GeV K_L^0	26
2.19	Jet energy resolution as a function of sampling frequency in the HCal. . .	28
2.20	Jet energy resolution as a function of sampling frequency in the HCal. . .	29
2.21	Jet energy resolution breakdown as a function of HCal sampling frequency for 45 and 250 GeV jets.	29

2.22	Energy resolution as a function of HCal sampling frequency for 50 GeV K_L^0	30
2.23	Jet energy resolution as a function of magnetic field strength.	31
2.24	Jet energy resolution breakdown as a function of magnetic field strength for 45 and 250 GeV jets.	32
2.25	Jet energy resolution as a function of ECal inner radius.	33
2.26	Jet energy resolution breakdown as a function of ECal inner radius for 45 and 250 GeV jets.	34

List of tables

2.1	Nominal ILD detector model ECal configuration.	13
2.2	Transverse segmentation layout of the ECal models considered.	17
2.3	Nominal ILD detector model HCal configuration.	20
2.4	Sampling fraction of HCal models considered.	27
2.5	Transverse segmentation layout of various HCal models considered. .	28